Spectrally resolved fluxes derived from collocated AIRS and CERES measurements and their application in model evaluation: Clear sky over the tropical oceans

Xianglei Huang,[1] Wenze Yang,[1,2] Norman G. Loeb,[3] and V. Ramaswamy[4]

[1] Spectrally resolved outgoing thermal-IR flux, the integrand of the outgoing longwave radiation (OLR), has a unique value in evaluating model simulations. Here we describe an algorithm for deriving such clear-sky outgoing spectral flux through the entire thermal-IR spectrum from the collocated Atmospheric Infrared Sounder (AIRS) and the Clouds and the Earth's Radiant Energy System (CERES) measurements over the tropical oceans. On the basis of the predefined scene types in the CERES Single Satellite Footprint (SSF) data set, spectrally dependent ADMs are developed and used to estimate the spectral flux each AIRS channel. A multivariate linear prediction scheme is then used to estimate spectral fluxes at frequencies not covered by the AIRS instrument. The whole algorithm is validated using synthetic spectra as well as the CERES OLR measurements. Using the GFDL AM2 model simulation as a case study, applications of the derived clear-sky outgoing spectral fluxes in model evaluation are illustrated. By comparing the observed spectral fluxes and simulated ones for the year of 2004, compensating errors in the simulated OLR from different absorption bands are revealed, along with the errors from frequencies within a given absorption band. Discrepancies between the simulated and observed spatial distributions and seasonal evolutions of the spectral fluxes are further discussed. The methodology described in this study can be applied to other surface types as well as cloudy-sky observations and also to corresponding model evaluations.

1. Introduction

[2] As an entity, the global mean outgoing longwave flux (commonly known as outgoing longwave radiation, hereafter OLR) reflects how the climate system balances the net incoming solar radiation at the top of atmosphere (TOA). Being one type of energy flux, OLR consists of an integrated contribution of radiance intensities at different frequencies and from different directions, which in turn is determined by various atmospheric and surface parameters such as atmospheric temperature and humidity profiles, trace gas concentrations, surface temperature and emissivity, and clouds and aerosols. Owing to these facts, OLR has been long recognized by the climate community as an important quantity to

observe and simulate [*Allan et al.*, 2004; *Barkstrom*, 1984; *Harries et al.*, 2005; *Ramanathan et al.*, 1989; *Wielicki et al.*, 1996; *Wielicki et al.*, 2002]. Since the launch of ERBE (Earth Radiation Budget Experiments) satellites in the mid-1980s [*Barkstrom*, 1984], there have been numerous studies of using the broadband OLR measured by ERBE to evaluate general circulation models (GCMs), operational analysis and reanalysis products [e.g., *Allan et al.*, 2004; *Raval et al.*, 1994; *Slingo et al.*, 1998; *Slingo and Webb*, 1992; *Wielicki et al.*, 2002; *Yang et al.*, 1999]. However, the integrand of OLR, the spectrally resolved radiance intensity, has not been used as much as the broadband OLR in such studies primarily because of a lack of measurement.

[3] The spectrally resolved radiance has a unique value in evaluating climate models [*Goody et al.*, 1998]. So does the spectral flux. Using broadband observations to understand model deficiencies sometimes is not straightforward: individual model errors that contribute to the different spectral regions can compensate one another to make the understanding of the whole broadband deficiencies difficult. From this aspect, it is obvious that spectrally resolved quantities (radiance intensities or fluxes) are valuable in such evaluations. A recent study by *Huang et al.* [2006] illustrated how spectrally resolved radiances can be used to quantify the model bias

[1]Department of Atmospheric, Oceanic, and Space Sciences, University of Michigan, Ann Arbor, Michigan, USA.
[2]Now at Hunter College, City University of New York, New York, USA.
[3]Radiation and Climate Branch, NASA Langley Research Center, Hampton, Virginia, USA.
[4]Geophysical Fluid Dynamics Laboratory, NOAA, Princeton University, Princeton, New Jersey, USA.

previously seen from a comparison between the ERBE-observed and model-simulated clear-sky broadband OLR (hereafter, OLRc). By comparing simulated spectra with IRIS (Infrared Interferometer Spectrometer) spectra collected during April 1970 to January 1971, they disclosed compensating errors arising from different absorption bands in the OLRc simulated by AM2, the new GFDL atmospheric GCM [*GFDL Global Atmosphere Model Development Team*, 2004]. Bias originating from the stratosphere can also be identified by examining infrared channels primarily sensitive to the stratospheric emissions. The IRIS data set covers only a period of 10 months with sparse spatial sampling. Nevertheless, because auxiliary information about each individual IRIS footprint is not available, *Huang et al.* [2006] had to use a single statistical regression scheme to do the radiance-to-flux conversion for all IRIS clear-sky spectra. Owing to these limitations, *Huang et al.* [2006] had to focus mostly on the bias of the monthly mean clear-sky OLR averaged over the entire tropical oceans. A more recent study by *Huang et al.* [2007] compares the simulated global-mean nadir-view radiances from September 2002 to October 2003 by the AM2 model with the counterparts observed by the Atmospheric Infrared Sounder (AIRS). Their result suggests that a seemingly good agreement between the model's global-mean broadband OLR and the observed may be due to cancellation of spectral errors.

[4] The Atmospheric Infrared Sounder (AIRS) [*Aumann et al.*, 2003; *Chahine et al.*, 2006] and the Clouds and the Earth's Radiant Energy System (CERES) [*Wielicki et al.*, 1996] aboard NASA Aqua satellite provide a timely opportunity of advancing the application of such spectrally resolved observations in model evaluations. The AIRS instrument records IR spectra over a wide spectral range while the CERES can provide measurements of the broadband OLR. In order to convert unfiltered radiance to the broadband OLR, the CERES team has categorized individual footprints to different scene types and developed a sophisticated angular distribution model (ADM) for each scene type [*Loeb et al.*, 2005; *Loeb et al.*, 2003]. This greatly facilitates the estimation of spectral flux at each AIRS channel since the CERES scene type information can be directly used to construct appropriate ADMs for each AIRS channel. Since AIRS does not have a full coverage of the whole IR region, the broadband OLR estimated from the AIRS radiances can then be validated against the collocated CERES OLR. Moreover, the AIRS and CERES on Aqua have been collecting data since July 2002. AIRS records ∼2.9 million spectra per day and the CERES instrument in the cross-track scan mode alone obtains ∼2.4 million measurements per day. Such dense sampling patterns imply that besides the monthly mean spectral flux over a broad climate zone, detailed spatial distributions and temporal evolutions of the spectral flux can be examined and compared with model simulations. Moreover, with spectral fluxes derived for both all-sky and clear-sky observations, band-by-band longwave cloud radiative forcing (LW CRF, the difference between clear-sky and all-sky flux) at the TOA can be obtained. Such spectrally dependent cloud radiative forcing can be used as a more stringent metric to assess the simulation of clouds in the GCMs than the broadband cloud radiative forcing by itself.

[5] The focus of this study is the clear-sky outgoing spectral flux over the tropical oceans and its application in model evaluation. The derivations of cloudy-sky spectra fluxes and hence band-by-band longwave cloud radiative forcing, as well as their applications in model evaluation, will be presented in a separate study. The remaining sections are organized in the following manner. Section 2 describes the data sets and models used in this study. The algorithm for deriving spectral fluxes over the entire thermal-IR spectrum from the collocated AIRS and CERES observations is depicted in section 3. Validation of this algorithm is discussed in section 4. Section 5 presents a case study of using the derived spectral fluxes to evaluate GCM simulations. Conclusions and further discussions are given in section 6.

2. Data Sets and Models

2.1. CERES

[6] The NASA *Aqua* spacecraft carries two identical CERES instruments (FM3 and FM4) [*Parkinson*, 2003]. Aqua is in a Sun-synchronous orbit 705 km above the surface. The instrument field of view (IFOV) of CERES is about 1.63 degrees, corresponding to a 20 km nadir-view footprint on the surface. At any given time, one CERES instrument is placed in a cross-track scanning mode and the other in either a rotating azimuth scanning or a programmable azimuth plane mode. Given that AIRS is operating in a cross-track scan mode, only CERES observations from the cross-track scanning mode are used in this study. The CERES instruments measure filtered radiances in the shortwave (SW, 0.3–5 μm), total (0.3–200 μm), and window (WN, 8–12 μm) regions. The filtered radiances are then converted to unfiltered reflected solar, unfiltered LW and WN radiances [*Loeb et al.*, 2001]. Corresponding fluxes are derived based on these unfiltered radiances and corresponding angular distribution models (ADMs).

[7] The CERES data set used in this study is the Aqua-CERES level 2 footprint data product, the Single Satellite Footprint (SSF) TOA/Surface Fluxes and Clouds Edition 2A [*Loeb et al.*, 2005]. The CERES SSF broadband fluxes are obtained from directional radiance measurements using a new generation of angular distribution models (ADMs) [*Loeb et al.*, 2005, 2007]. For clear sky footprints over the oceans, the scene type of interest in this study, it is further stratified into discrete intervals of precipitable water retrieved from SSM/I (Special Sensor Microwave Imager) [*Goodberlet et al.*, 1990], vertical temperature change in the first 300 hPa of the atmosphere above the surface as derived from GEOS Data Assimilation System [*DAO*, 1996], and image-based surface skin temperature. ADM is constructed for each discrete interval. Using these ADMs significantly reduces both the bias and the root-mean square (RMS) errors of LW TOA flux. *Loeb et al.* [2007] estimated a bias of 0.2–0.4 Wm^{-2} and RMS error < 0.7 Wm^{-2} for Aqua-CERES regional mean LW TOA flux.

2.2. AIRS and the Collocation Strategy

[8] AIRS is an infrared grating array spectrometer aboard *Aqua* [*Aumann et al.*, 2003]. It records spectra at 2378 channels across three bands (3.74–4.61 μm, 6.20–8.22 μm, 8.8–15.4 μm) with a resolving power ($\lambda/\Delta\lambda$) of 1200.
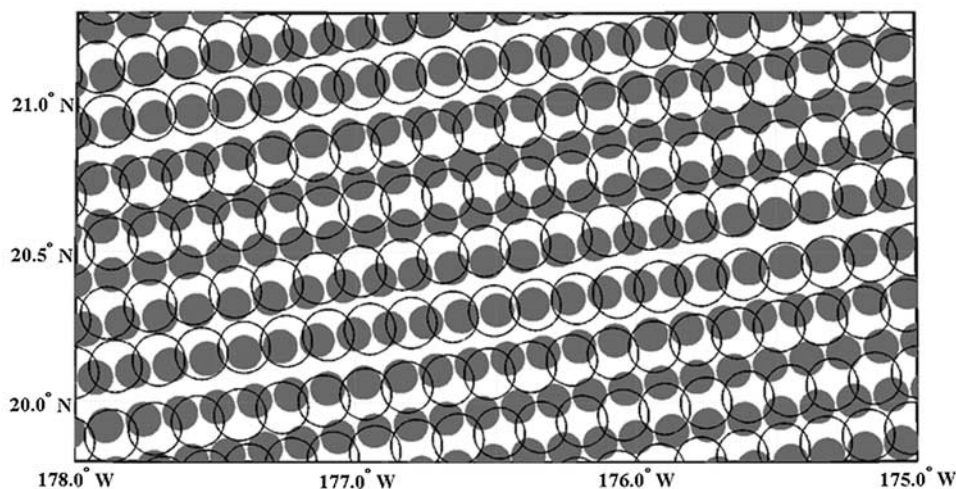
Figure 1. The surface footprints of AIRS (solid gray circles) and CERES (open black circles) as observed from about 0106:15 to 0106:45 UTC on 1 January 2005.

AIRS scans from $-49°$ to $49°$ with an IFOV of 1.1 degrees, corresponding to a nadir-view footprint of 13.5 km on the surface. The in-flight calibrations show a radiometric accuracy of <0.3 K for a 250 K brightness temperature target [*Pagano et al.*, 2003] and a spectral accuracy of <0.01Δv (here Δv is the full width at half maximum of each channel) [*Gaiser et al.*, 2003]. AIRS collects ~2.9 million spectra per day and global coverage can be obtained in the course of two days. It provides an unprecedented data source of the outgoing thermal IR spectra with excellent calibration and good global coverage.

[9] In this study we use the AIRS geolocated and calibrated radiances (level 1B). Among the 2378 AIRS channels, only those recommended by the AIRS team for level-2 retrieval purposes are used. Modern GCMs usually parameterize the longwave radiation up to about 2000 cm^{-1} (e.g., both the GFDL AM2 and the NCAR CAM3 models use 2200 cm^{-1} as the upper bound of longwave spectral range). Therefore, AIRS radiances from the $3.74-4.61$ μm (2169–2673 cm^{-1}) band are not used in this study and the spectral fluxes are derived only for 10–2000 cm^{-1}. In addition, we screen the data with a strict quality control procedure to exclude possible bad spectra as done in the work of *Huang and Yung* [2005].

[10] Figure 1 shows part of AIRS and CERES FM4 (in cross-track scanning mode) footprints as sampled from 0106:15 to 0106:45 UTC on 1 January 2005. For each cross-track scanning track, AIRS records 90 spectra with scan angle between ±49° while CERES processes the same number of measurements with view zenith angles no more than 65.8°. At nadir view, the area of an AIRS footprint is about 45% of that of a CERES footprint. As a result, many AIRS footprints are either completely or largely overlapped within corresponding CERES footprints. As we shall see in later sections, such overlapped measurements, a subset of both AIRS and CERES data, can still render meaningful gridded regional products. For collocated AIRS and CERES footprints, the scene type information of the CERES footprint and relevant auxiliary information stored in CERES SSF products can be largely applied to the AIRS pixel.

Therefore, such a collocation greatly facilitates the conversion from the AIRS radiances to spectral fluxes. The collocation criteria adopted in this study are (1) the time interval between AIRS and CERES observations is within 8 s, and (2) the distance between the center of an AIRS footprint and that of a CERES footprint on the surface ($\Delta_{airs-ceres}$) is less than 3 km. The second criterion ensures that the major portion of AIRS footprint is within the collocated CERES footprint even for a large scan angle. For example, at a scan angle of 45° and $\Delta_{airs-ceres} = 3$ km, an AIRS footprint still has at least a 50% overlapping with the collocated CERES footprint. In practice, we only use AIRS data with scan angles within ±45°.

2.3. Models

[11] In order to construct ADMs suitable for the AIRS and estimate spectral fluxes at frequencies not covered by the AIRS instrument, a forward radiative transfer model is needed. We use MODTRAN^{TM}-5 version 2 revision11 (hereafter, MODTRAN5) for this purpose. MODTRAN^{TM}-5 was collaboratively developed by Air Force Research Laboratory and Spectral Sciences Inc. [*Berk et al.*, 2005]. Mod5v2r11 is based on HITRAN2K line compilation with updates through 2004 [*Rothman et al.*, 2005; *Rothman et al.*, 1998]. Compared to the previous versions of MODTRAN band model [*Berk et al.*, 1998; *Bernstein et al.*, 1996], MODTRAN5 inherits the flexibility in handling clouds and significantly improves the spectral resolution to as fine as 0.1 cm^{-1}. Comparisons between this model and line-by-line radiative transfer model, LBLRTM [*Clough and Iacono*, 1995; *Clough et al.*, 2005], show agreement up to a few percent or better in the thermal IR transmittances and radiances [*Anderson et al.*, 2006]. These features make MODTRAN5 well suited for simulating AIRS radiances [*Anderson et al.*, 2006; *Feldman et al.*, 2006]. In this study, synthetic AIRS spectrum is done by convolving the MODTRAN5 output at 0.1 cm^{-1} resolution with the spectral response functions of individual AIRS channels [*Strow et al.*, 2006; *Strow et al.*, 2003].

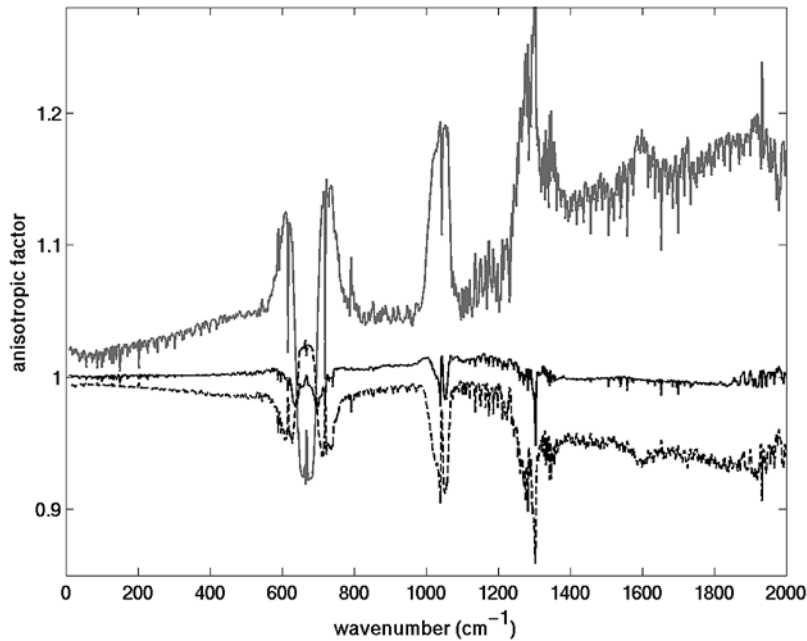[12] For illustrating the application of derived spectral fluxes in model evaluation, we use a version of AM2

Figure 2. The spectrally dependent anisotropic factors based on the U.S. 1976 standard atmosphere profile. The solid gray line is for $0°$ zenith angle and the black dashed line is for $60°$ zenith angle. The upwelling flux is the top-of-atmosphere (TOA) flux. For comparison, the spectrally dependent anisotropic factors for $52.96°$ zenith angle (corresponding to the diffusivity factor of 1.66) are plotted in the black solid line.

(am2p14), the atmospheric GCM recently developed at NOAA Geophysical Fluid Dynamics Lab (GFDL). It employs a hydrostatic, finite volume dynamical core with $2.5°$ longitude by $2°$ latitude horizontal resolution and 24 vertical levels, the top level being at ~ 3 hPa. Cloud quantities such as cloud liquid water, cloud ice amount, and cloud fraction are treated as prognostic variables. The relaxed Arakawa-Schubert scheme is used for cumulus parameterization with several modifications. The shortwave and the longwave radiation parameterizations follow *Freidenreich and Ramaswamy* [1999] and *Schwarzkopf and Ramaswamy* [1999], respectively. The longwave radiation parameterization computes radiative fluxes at eight spectral ranges. The TOA flux at each spectral range can be directly evaluated against the counterparts derived from the collocated AIRS and CERES observations. A detailed description of AM2 can be found in the work of *GFDL Global Atmosphere Model Development Team* [2004].

[13] The AM2 model is forced by observed monthly SSTs from 2002 to 2006. Ozone is prescribed at its 1990s level based on a combined data set of observed stratospheric [*Randel and Wu*, 2007] and simulated tropospheric [*Horowitz*, 2006] ozone distributions. Observed CO_2 and other greenhouse gas concentrations appropriate for the period are used in the run. Three-hourly instantaneous outputs are archived from the simulation. To minimize the temporal sampling difference from the collocated AIRS-CERES data set, the 3-hourly instantaneous outputs are further interpolated to the same time and location as those collocated AIRS-CERES observations identified in section 2.2. Besides the radiative fluxes over eight spectral ranges directly output from the AM2 model, the subsampled temperature and humidity profiles are fed into the MODTRAN5 to obtain spectral fluxes at every 10 cm^{-1}

intervals from 10 to 2000 cm^{-1}. Such 10 cm^{-1} spectral flux will also be compared with the counterpart derived from the collocated AIRS and CERES measurements.

3. Algorithm

[14] Since we are interested in using AIRS observations to derive the spectral fluxes over the whole IR region, two issues must be addressed: (1) estimating the spectral flux at each AIRS channel and (2) estimating the spectral fluxes at frequencies not covered by the AIRS instrument. Sections 3.1 and 3.2 describe solutions to the two issues, respectively.

3.1. Spectrally Dependent ADMs

[15] An angular distribution model is needed to covert directional radiance measurement to flux. The central quantity in such conversion is the anisotropic factor, which is defined as

$$R_v(\theta) = \frac{\pi I_v(\theta)}{F_v} \qquad (1)$$

where $I_v(\theta)$ is the TOA upwelling radiance at frequency v along zenith angle θ and F_v is the TOA upwelling spectra flux at frequency v. Compared to the broadband anisotropic factor used in CERES ADMs, here R is not only a function of θ but a function of v.

[16] Figure 2 shows $R_v(\theta)$ of the United States 1976 standard atmosphere profile computed by the MODTRAN5 with a spectral resolution of 2 cm^{-1} for three zenith angles, $0°$, $60°$, and $52.96°$ (the diffusive angle corresponding to the diffusivity factor of 1.66), respectively. At most wave numbers, $R_v(\theta)$ decreases with viewing zenith angle, a

Table 1. The 14 Discrete Intervals of Precipitable Water (pw), Lapse Rate (ΔT, Defined as the Vertical Temperature Change of the First 300 hPa Above the Surface), and Surface Skin Temperature (T_s) Used in the CERES LW ADMs to Determine Clear-Sky OLR Over the Oceans

Discrete Interval	pw(cm)	ΔT(K)	T_s (K)
1	0–1	<15	270–290
2	0–1	<15	290–310
3	0–1	15–30	270–290
4	0–1	15–30	290–310
5	1–3	<15	270–290
6	1–3	<15	290–310
7	1–3	15–30	270–290
8	1–3	15–30	290–310
9	1–3	15–30	310–330
10	3–5	<15	270–290
11	3–5	<15	290–310
12	3–5	15–30	290–310
13	>5	<15	290–310
14	>5	15–30	290–310

dependence often referred to as "limb-darkening." For all angles, the anisotropic factors in the atmospheric window regions (850–1000 cm^{-1}, 1100–1200 cm^{-1}) and the water vapor pure rotational band (<500 cm^{-1}) are closer to one than those in other bands. The limb-darkening is stronger in the ozone band (990–1070 cm^{-1}), the Q-branch of methane band (~1306 cm^{-1}), and the water vapor ν_2 band (1200–2000 cm^{-1}). In contrast, $R_\nu(\theta)$ increases with viewing zenith angle in the center of the CO$_2$ band (~667 cm^{-1}), corresponding to "lime-brightening." The contrast between the CO$_2$ band and other bands is primarily due to the fact that the effective emission levels for channels at the CO$_2$ band center are located in the stratosphere rather than in the troposphere. The larger the viewing zenith angle (θ), the higher the effective emission level. As temperature increases with the height in the stratosphere, this leads to a larger radiance intensity when θ becomes larger. Therefore, if we define the frequency-dependent diffusive angle, θ_{diff}, as $\pi I_\nu(\theta_{diff}) = F_\nu$, then, for any $\theta < \theta_{diff}$, $R_\nu(\theta)$ will be smaller than one; for any $\theta > \theta_{diff}$, $R_\nu(\theta)$ will be larger than one. In the troposphere, temperature decrease with the altitude, which means that the opposite dependence of $R_\nu(\theta)$ on θ will occur.

[17] As mentioned in section 2.1 and 2.2, necessary scene type information can be retrieved from the CERES SSF product and then the scene type is directly applicable to the collocated AIRS observation. According to Table 3 in the work of *Loeb et al.* [2005], clear-sky conditions over all surface types are further stratified to 80 discrete intervals of precipitable water (pw), lapse rate (ΔT), and surface skin temperature (T_s). In practice, it turns out that only 14 out of the 80 intervals are needed to accommodate all possible clear-sky scenes observed over the oceans, which are listed in detail in Table 1. Since we focus on tropical ocean regions in this study, we only need to construct appropriate spectral ADMs for the 14 intervals.

[18] We use 6-hourly profiles from the ECMWF ERA-40 reanalysis [*Uppala et al.*, 2005] in conjunction with the MODTRAN5 to derive the spectral ADMs for all 14 intervals in the following way. Four months of ECMWF data (October 2001, January 2002, April 2002, and July 2002) are used. For each month, four 6-hourly time intervals are chosen. For each selected 6-hourly period, temperature,

and humidity profiles between 60°S–60°N oceans are fed into the MODTRAN5 to compute anisotropic factors of individual AIRS channels for zenith angles from 0° to 45°. By doing so, 80,640 profiles and associated synthetic AIRS spectra and anisotropic factors are archived. These profiles and anisotropic factors are then categorized into discrete intervals of pw, ΔT, and T_s as listed in Table 1. The mean anisotropic factor from all samples belonging to a discrete interval is defined as the anisotropic factor for that interval. By doing so, spectrally dependent ADMs for converting AIRS radiances to spectra fluxes are constructed. Meanwhile, broadband ADMs can also be obtained and checked with the CERES ADMs for consistency. For each discrete interval, the CERES ADMs use a pair of slightly different anisotropic factors (~0.1–0.4% difference in fraction), one for the daytime scenes and the other for the nighttime scenes. Figure 3 shows a pair of such CERES anisotropic factors for a given discrete interval (the gray solid lines with diamonds and circles). The corresponding broadband anisotropic factors derived from the aforementioned procedure are also shown in Figure 3 (black dash line). The three curves closely follow each other with little differences. The differences between the derived and the CERES daytime anisotropic factor are −0.1%–0.2%. For the CERES nighttime anisotropic factor, the differences range from −0.2% to −0.1%.

3.2. Estimating Spectral Fluxes at Frequencies Not Covered by AIRS

[19] In order to obtain spectral fluxes over the entire thermal-IR spectral range, a scheme has to be developed to estimate spectral fluxes at frequencies without the AIRS coverage. AIRS has no coverage at frequencies lower than 649.6 cm^{-1} and between 1613.9 and 2000 cm^{-1}. AIRS has
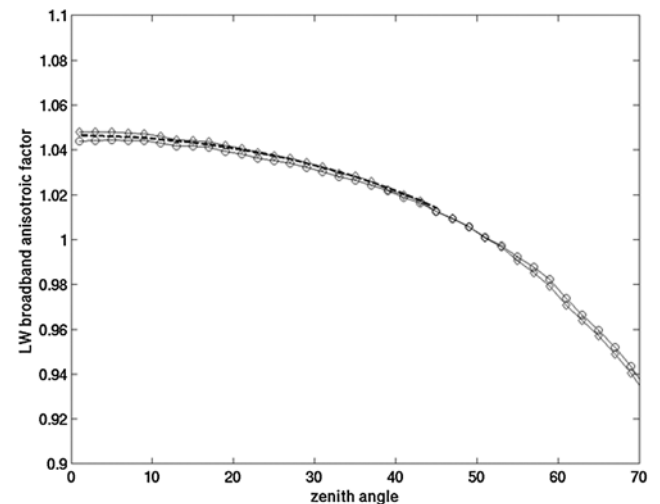

Figure 3. The solid line with diamonds is LW broadband anisotropic factor used in the CERES SSF product for the daytime clear-sky scenes over the ocean with $pw = 1-3$ cm, $\Delta T < 15$ K, and $T_s = 290–310$ K (discrete interval 6 in Table 1). The solid line with circles is used for the corresponding nighttime clear-sky scenes. The thick dashed line is the LW broadband anisotropic factor derived from the procedure described in section 3.1.

12 modules assembled on the focal plane [*Aumann et al.*, 2003], each having its own spectral range. The spectral ranges of neighbor modules might overlap with each other. As a result, a few spectral ranges are sampled by more than one module. Meanwhile, the modules do not provide a continuous coverage from 649.6 cm^{-1} and 1613.9 cm^{-1}. For example, no AIRS channel covers 1136.6–1217.0 cm^{-1} and 1046.2–1056.1 cm^{-1}. To address the spectral coverage issue, the following strategy is adopted to cover the entire spectral range from 10 cm^{-1} to 2000 cm^{-1}:

[20] 1. For the spectral range continuously covered by AIRS, AIRS channel frequency is used. For the spectral range sampled by two overlapped channels, only one channel is kept and used in later analysis.

[21] 2. Frequency gaps between 649.6 cm^{-1} and 1613.9 cm^{-1} are covered with channels having the same spectral resolution as the nearest AIRS channels.

[22] 3. For 10cm^{-1} to 649.6 cm^{-1}, it is covered with channels at a spectral resolution of 0.5 cm^{-1}, approximately the same resolution as the nearest AIRS channel.

[23] 4. For 1613.9 cm^{-1} to 2000cm^{-1}, it is covered with channels at a spectral resolution of 1.5 cm^{-1}, approximately the same resolution as the nearest AIRS channel.

[24] Hereafter, the above four sets of channels are referred to as channel sets 1–4, respectively.

[25] For AIRS channels in set 1, radiance $I_\nu(\theta)$ can be converted to the spectral flux F_ν using the spectrally dependent ADMs described in section 3.1. For channels in the sets of 2–4, a multiregression scheme based on the Principal Component Analysis is used to obtain the corresponding spectra fluxes. Parameters in the regression scheme are derived based on the ECMWF profiles and synthetic spectra mentioned in section 3.1. For every ECMWF profile falling into a given discrete interval of (pw, ΔT, T_s), the synthetic spectral fluxes at all channels set 1–4 are computed. Spectral EOF analysis (principal component analysis in the spectral domain) [*Haskins et al.*, 1999; *Huang et al.*, 2003; *Huang and Yung*, 2005] is applied to the collection of synthetic spectral fluxes to derive a set of orthogonal basis in the frequency domain,

$$F_\nu = \overline{F}_\nu + \sum_{j=1}^{N} e_j \phi_\nu^j \qquad (2)$$

where F_ν is the synthetic spectral flux at frequency ν from one ECWMF profile and $\overline{F}_\nu$ is the average of all synthetic spectral fluxes at ν. N is the total number of channels, $\phi_\nu^j (j = 1 - N)$ are the principal components (unit vectors) that consist of a complete set of orthogonal basis in the N-dimensional space, and e_j is the projection of $(F_\nu - \overline{F}_\nu)$ onto the jth principal component ϕ_ν^j. In practice, it is found that 99.99% variance can be explained by the first 20 or even less principal components. Therefore, we only retain the first M principal components that account for 99.99% variance. In the matrix form, it means

$$\mathbf{F} - \overline{\mathbf{F}} \approx [\phi^1, \phi^2, \ldots, \phi^M] \begin{bmatrix} e_1 \\ e_2 \\ \cdots \\ e_M \end{bmatrix} = \mathbf{\Phi}e \qquad (3)$$

where $\mathbf{F}$, $\overline{\mathbf{F}}$, ϕ^1, …, $\phi^\grave{1}$ are vectors with a dimension of $N (N \gg M)$. Correspondingly, Φ is an N × M matrix and $\mathbf{e}$ is an M × 1 vector. Note that the total number of channels in channel sets 1–4 is N. The total number of AIRS channels (N_{AIRS}) is smaller than N but much larger than M.

[26] Since (3) holds for all channels, if we use AIRS in subscript to denote a set of valid AIRS channels, we still have

$$\mathbf{F}_{AIRS} - \overline{\mathbf{F}}_{AIRS} \approx \mathbf{\Phi}_{AIRS}\mathbf{e} \qquad (4)$$

[27] Note that $\mathbf{F}_{AIRS}$ could be derived from AIRS measurement as described in section 3.1. $\overline{\mathbf{F}}_{AIRS}$, on the other hand, are the mean spectral fluxes at the AIRS channels as derived from the set of synthetic spectra mentioned before. Equation (4) implies a least-square solution

$$\mathbf{e} \approx \left(\mathbf{\Phi}_{AIRS}^* \mathbf{\Phi}_{AIRS}\right)^{-1} \mathbf{\Phi}_{AIRS}^* \left(\mathbf{F}_{AIRS} - \overline{\mathbf{F}}_{AIRS}\right) \qquad (5)$$

where Φ^* is the transpose of Φ;. Once $\mathbf{e}$ is obtained for every qualified AIRS observation, (3) can be used to derive the spectral flux at each channel in sets 1–4, the channel sets not covered by the AIRS instrument. In practice, because of $N_{AIRS} \gg M$, $\mathbf{\Phi}_{AIRS}$ is well-conditioned for every discrete intervals of (pw, ΔT, T_s) and inversion of ($\mathbf{\Phi}^*_{AIRS} \mathbf{\Phi}_{AIRS}$) is numerically stable.

[28] In summary, this method finds the least-square-fit of the projections of AIRS-derived spectral fluxes onto the principal components. Similar multivariate regression technique has been used before to reconstruct global-scale temperature patterns over the last six centuries [e.g., *Mann et al.*, 1998]. While *Mann et al.* [1998] used this technique to fill missing spatial information, we used it here to fill missing spectral information. In practice, an AIRS channel could suffer from background electronic noise and, as a result, it might provide meaningful observations most of the time but could occasionally go wrong. This method is well suited for such situation since it only needs a subset of AIRS channels with valid calibrated radiances. Thus, it can tolerate a varying set of qualified channels from measurement to measurement. It makes use of information from all available good channels yet avoids the painstaking error handling of bad channels for each individual measurement. A chart summarizing the whole algorithm described in section 3.1 and 3.2 is shown in Figure 4.

4. Validation

[29] Validating the algorithm described in section 3 is done in two parts. The first part is "theoretical validation," synthetic AIRS spectra are used to derive the spectral fluxes and such spectral fluxes are compared with those directly computed from the MODTRAN5. The second part is using the algorithm to derive the broadband OLR from the AIRS spectrum and compare it with the collocated CERES OLR. The first part lets us assess the whole algorithm without concerning the accuracy in spectroscopy and forward modeling since the MODTRAN5 is used as a surrogate of radiative transfer in the real world. The second part is more rigorous in the sense that all realistic uncertainties, such as
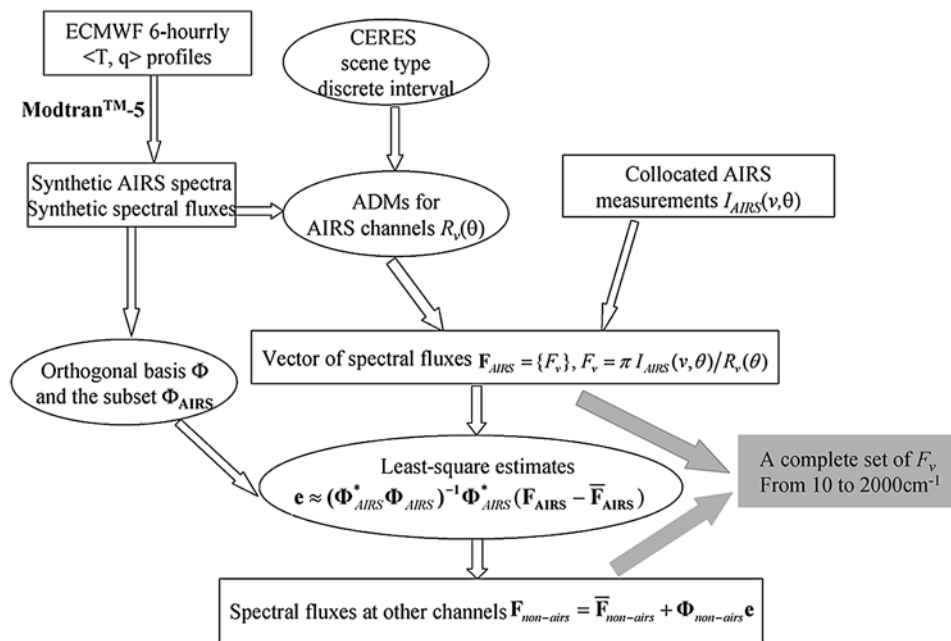
Figure 4. Flowchart illustration of the algorithm of deriving spectral fluxes from 10 cm^{-1} to 2000 cm^{-1} from the collocated AIRS and CERES measurements. Notations are the same as those defined in the context (section 3).

those in spectroscopy, forward modeling, and collocation strategies, are taken into account.

4.1. Theoretical Validation

[30] ECMWF ERA-40 6-hourly temperature and humidity profiles over the oceans between 60°S–60°N in 1999 February (a different year and a different month from those ECMWF data used in section 3) are randomly selected, classified to appropriate discrete intervals, and then synthetic AIRS spectra at different zenith angles and LW spectral fluxes are computed from the MODTRAN5. For each discrete interval, about 400 random samples are archived. The differences between the spectral fluxes (or the broadband OLR) predicted from the synthetic AIRS spectra and the ones directly computed from the MODTRAN5 are examined. Figure 5 shows such differences for three different viewing zenith angles: 0°, 21°, and 45°. For all three angles, the mean differences for any discrete interval are generally within ±0.5 Wm^{-2}. The standard deviations are no more than 1.5 Wm^{-2}. The maximum and minimum differences from the individual comparisons are within ±5 Wm^{-2}. The differences have no noticeable dependence on either the zenith angle or the discrete interval. The OLR differences for other viewing zenith angles are consistent with what is shown in Figure 5.

[31] Besides the difference in the broadband OLR, the differences between the "predicted" and the "directly computed" spectra fluxes are also examined. Figure 6 shows the mean differences of spectral fluxes for each ADM discrete interval and one viewing zenith angle (21°). For all spectral intervals shown in Figure 6, 93% of them has a mean difference within ±0.02W/(m$^2 \times$ 10 cm^{-1}) and 98.7% of them has a mean difference within ±0.05W/(m$^2 \times$ 10 cm^{-1}). The largest absolute differences are seen mostly in two ADM discrete intervals (intervals 4 and 9;

refer to Table 1 for the definitions of these intervals), which are no more than ±0.06W/(m$^2 \times$ 10 cm^{-1}) (in fraction, no more than ±5%). The bias patterns for other viewing zenith angles (not shown here) are similar to Figure 6. The good agreement between the "predicted" and the "directly computed" spectral fluxes indicates that when the uncertainties in spectroscopy parameters and radiative transfer modeling are excluded, the algorithm is capable of obtaining spectral fluxes at 10 cm^{-1} intervals with enough confidence.

4.2. Comparison With Collocated CERES Observations

[32] In order to test the performance of the algorithm, we collocate the AIRS spectra measured over the tropical oceans (30°S–30°N) in 2004 with the CERES cross-track clear-sky measurements, apply our algorithm to derive the broadband OLR (OLR$_{AIRS}$), and then compare with the collocated CERES broadband OLR (OLR$_{CERES}$). A CERES field of view (FOV) is deemed as clear sky if the coincident MODIS pixel-level cloud coverage within the CERES FOV is ≤0.1% [*Geier et al.*, 2001; *Loeb et al.*, 2003]. In total, ~13.48 million of collocated AIRS and CERES measurements over the tropical ocean in the entire year of 2004 are identified based on our collocating criteria. Among these measurements, ~1.076 million (~8.0%) are classified as clear sky according to the CERES algorithm. Figure 7 shows the histogram of OLR$_{AIRS}$-OLR$_{CERES}$ differences for all 1.076 million collocated individual clear-sky measurements. The histogram approximates Gaussian distribution with a mean of 0.67 Wm^{-2} and a standard deviation of 1.52 Wm^{-2} (for comparison, a typical value of tropical clear-sky OLR is 287 Wm^{-2}), indicating that the OLR derived from our algorithm is highly consistent with the CERES OLR.
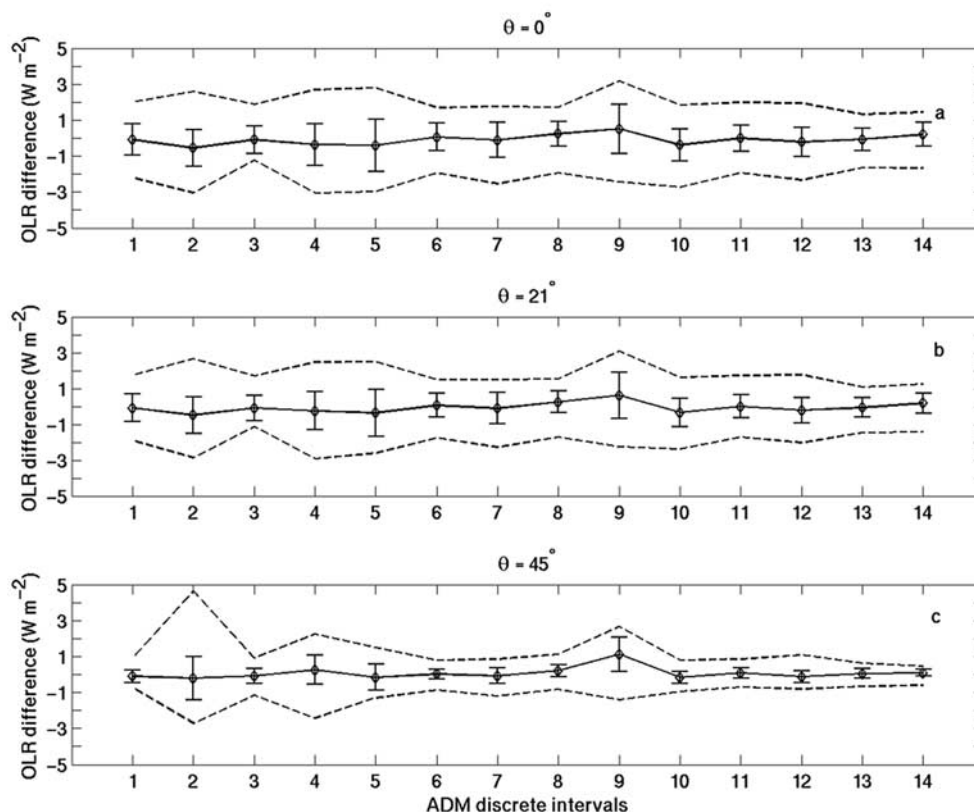
Figure 5. (a) Difference between the OLR predicted from the synthetic nadir-view AIRS spectra ($0°$ zenith angle) and directly computed OLR from MODTRAN™-5 for 14 discrete intervals of CERES clear-sky ADMs listed in Table 1. Four hundred profiles randomly selected from ECMWF data sets are used for each discrete interval. The diamond is the mean difference, the error bar shows the mean $\pm$ standard deviation, the dashed lines are the maximum and minimum differences for all random profiles in a given discrete interval. (b) Same as Figure 5a except the zenith angle of $21°$. (c) Same as Figure 5a except the zenith angle of $45°$.

[33] The collocated measurements are further divided into two groups: one in ascending node and the other in descending node. For each group, the clear-sky OLR (OLRc) derived from AIRS spectra are averaged onto $2.5°$ longitude by $2°$ latitude grid boxes (the same grid boxes as used in the GFDL AM2 model) on a daily basis. The collocated CERES OLRc are averaged in the same way. Further comparisons are conducted for such daily gridded OLRc.

[34] Given that CERES uses two sets of slightly different ADMs for ascending and descending measurements while we use one set of spectral ADMs for both ascending and descending measurements, the AIRS-CERES differences are further examined in two groups, ascending-node and descending-node, respectively. Figure 8a shows the differences between the daily gridded OLRc derived from the AIRS descending-node spectra (OLRc$_{AIRS}$) and the counterparts from the CERES SSF product (OLRc$_{CERES}$). The mean difference averaged over all valid grid boxes within the tropics is $0.83 Wm^{-2}$ with little day-to-day variation. The standard deviation of OLRc$_{AIRS}$-OLRc$_{CERES}$ is $\sim1.51 Wm^{-2}$, also with little daily variation. For a single grid box in the area of interest, the maximum daily differences ranges from 5 to $10 Wm^{-2}$ while the minimum from -3 to $-10 Wm^{-2}$. For the ascending node (Figure 8b), the mean

daily difference is $0.62 Wm^{-2}$ with little daily fluctuation and the standard deviation is $\sim1.16 Wm^{-2}$. The maximum and minimal differences are also within $\pm10 Wm^{-2}$.

[35] In summary, for both the theoretical validation and the AIRS-CERES comparison, the mean OLR differences are within $2 Wm^{-2}$ (<1% of tropical mean clear-sky OLR) and any individual difference is largely confined to within $\pm10 Wm^{-2}$. The mea OLR differences in theoretical validation show little dependence on view zenith angles and discrete intervals of scene types. The AIRS-CERES mean differences show consistent performance with little day-to-day fluctuation over the entire year. Therefore, we conclude that the algorithm is robust in estimating the broadband OLR. The theoretical validation for $10 cm^{-1}$ spectral fluxes show that, in an average sense, maximum discrepancies are within $\pm0.06 W/(m^2 \times 10 cm^{-1})$, about 5% of the TOA spectral fluxes over those spectral bins. This indicates the confidence of the algorithm in obtaining spectral fluxes at $10 cm^{-1}$ or even larger spectral intervals.

5. Application in Model Evaluation: A Case Study With the GFDL AM2 Simulation

[36] To illustrate the application of the derived spectral fluxes in GCM evaluation, we compare them with counter-
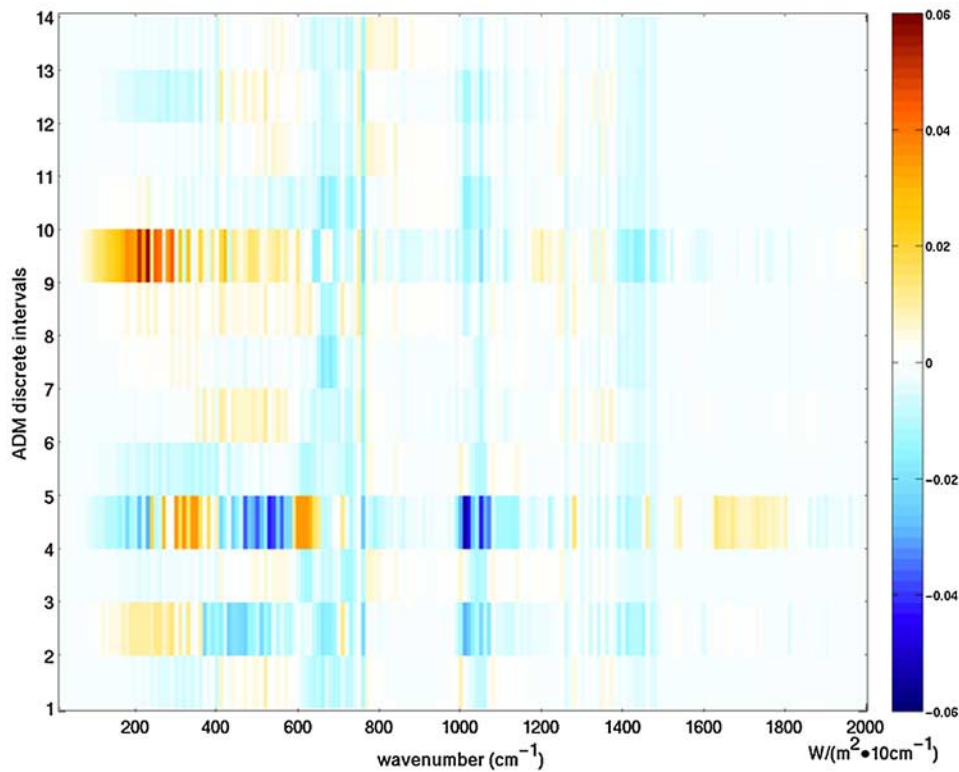
Figure 6. The mean difference between the predicted TOA spectra fluxes based on synthetic AIRS spectra and the directly computed TOA spectral fluxes from MODTRAN™-5 for each ADM discrete interval. The spectral flux is computed for every 10 cm^{-1} interval from 10 to 2000 cm^{-1}. Ordinate represents the 14 discrete intervals of CERES clear-sky ADMs listed in Table 1. Four hundred profiles randomly selected from ECMWF data sets are used to calculate the mean difference for each discrete interval. The unit of the mean difference is W per m^2 per 10 cm^{-1}.

parts from the AM2 model simulation over the same period as forced by observed sea surface temperature (SST). As mentioned in section 2, the output of AM2 simulation is further sampled to ensure consistent temporal and spatial sampling patterns with the observations. All comparisons are based on such a subsampled AM2 data set. For simplicity, all comparisons are done with data collected during the ascending node only. Similar conclusions can be reached when the descending data are examined. Occasionally, in order to contrast the differences between the AM2 model and observations, 6-hourly NCEP-DOE reanalysis data [Kanamitsu et al., 2002] for the year of 2004 is used to generate a "third-party" comparison. The 6-hourly NCEP-DOE reanalysis data is processed in the same way as the AM2 model output and corresponding synthetic spectral fluxes are computed from the MODTRAN5. Section 5.1 focuses on the band-by-band IR fluxes directly output from the AM2. Section 5.2 discusses the comparison at a finer spectral resolution, 10 cm^{-1} spectral interval.

5.1. Band-By-Band IR Fluxes

[37] The AM2 LW radiation parameterization scheme outputs the LW fluxes over eight different spectral ranges (bands) as listed in Table 2. In practice, two of them (0–560 cm^{-1}, 1400–2200 cm^{-1}) are treated together as a combined band. The absolute flux can vary by a factor up to 10 from one band to another band used in the AM2. To
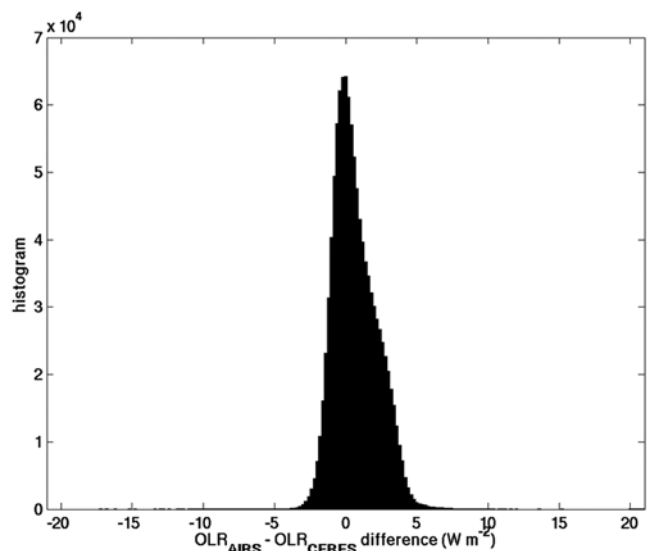

Figure 7. Histogram of differences between AIRS-derived OLR and CERES OLR for all individually collocated AIRS and CERES clear-sky footprints over the tropical oceans in 2004. In total 1.076 million collocated footprints are identified. The mean is 0.67 Wm^{-2} and the standard deviation is 1.52 Wm^{-2}.
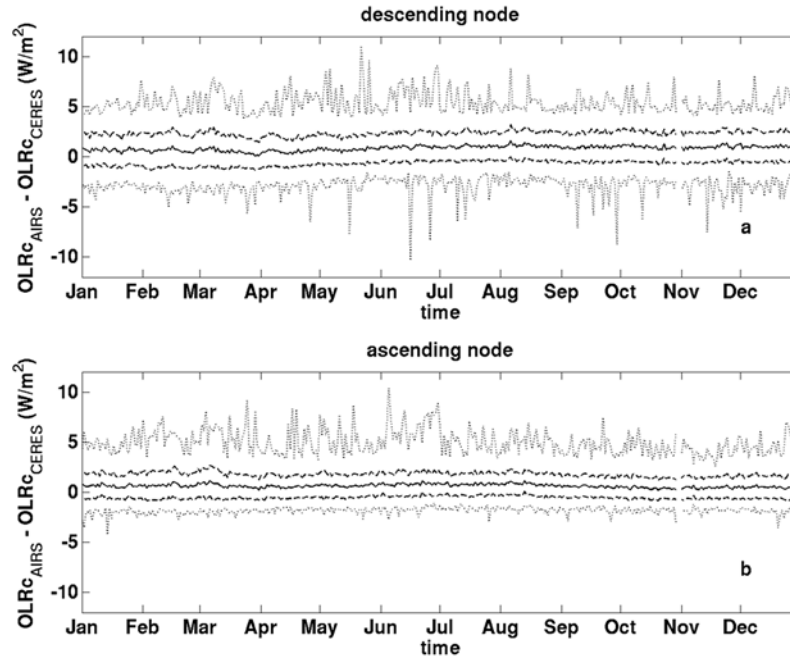
Figure 8. (a) The daily difference between the clear-sky OLR (OLRc) over the tropical oceans estimated from AIRS spectra measured during descending node and that from the collocated CERES measurement. The temporal coverage is from January to December of 2004. Individual collocated observations are gridded onto $2.5° \times 2°$ grid boxes on a daily basis before the difference is taken. The black solid line is the averaged daily difference over all grid boxes. The black dashed lines are the mean $\pm$ standard deviation. The gray dotted lines are the maximum and minimum differences for all grid boxes. (b) Same as Figure 8a except for the ascending node.

make a better comparison across all spectral bands, we focus on the clear-sky spectral greenhouse parameters [*Ackerman et al.*, 1992; *Frey et al.*, 1996] and the clear-sky broadband greenhouse parameters [*Raval and Ramanathan*, 1989] rather than the absolute spectral fluxes. The spectral greenhouse parameter is defined as

$$g_{\Delta v} = \frac{\int_{\Delta v} B_v(T_s)dv - F_{\Delta v}}{\int_{\Delta v} B_v(T_s)dv} \qquad (6)$$

where T_s is the surface temperature, Δv denotes the spectral range, $B_v(T_s)$ is the blackbody radiation at frequency v and temperature T_s, and $F_{\Delta v}$ is the clear-sky TOA outgoing flux over the same spectral range Δv. The spectral greenhouse parameter, $g_{\Delta v}$, is a measure of radiant energy over Δv trapped in the atmosphere. $g_{\Delta v} = 0$ when the atmosphere is transparent over Δv, and $g_{\Delta v} \rightarrow 1$ when atmosphere is opaque over Δv and emits to space at a temperature much colder than the surface temperature. When Δv spans over the whole LW region, $g_{\Delta v}$ becomes the broadband greenhouse parameter (hereafter, g_{LW}), representing the fraction of total radiant energy leaving the surface but trapped in the atmosphere.

[38] Figure 9a shows the 2004 annual-mean clear-sky broadband greenhouse parameter derived from the AM2 simulation. Intertropical Convergence Zone (ITCZ) and Southern Pacific Convergence Zone (SPCZ) are clearly associated with the maxima of clear-sky g_{LW} ($\sim 0.43-0.45$) because the two convergence zones tend to have higher humidity throughout the whole troposphere than

other areas. Meanwhile, the large-scale subsidence drying tends to decrease the humidity in the middle and upper troposphere while the entrainment of marine stratus tends to dry the lower-tropospheric layer just above its top [*Houze*, 1993]. Thus the minima of clear-sky g_{LW} (~ 0.30) can be seen off the west coasts of major continents where the marine stratus prevails and large-scale subsidence is prominent. The differences in the clear-sky g_{LW} between the AM2 and AIRS (Figure 9b) indicate that the AM2 overestimates g_{LW} over most of the tropical oceans and such overestimation, in general, is positively correlated with the g_{LW} itself. In the ITCZ and SPCZ, the overestimation could be as large as $0.035-0.04$ ($\sim 7.8-8.9\%$). Underestimations of g_{LW} by the AM2 happen in the subtropical oceans west of

Table 2. List of Eight Spectral Ranges at Which the AM2 LW Parameterization Schemes Directly Output the TOA Band-By-Band Fluxes

	Spectral Range (cm^{-1})	Primary Absorbers
1[a]	0−560	H_2O
2	560−800	CO_2, N_2O
3	800−900	H_2O continuum
4	900−990	H_2O continuum
5	990−1070	O_3
6	1070−1200	H_2O continuum
7	1200−1400	H_2O, CH_4, N_2O
8[a]	1400−2200	H_2O

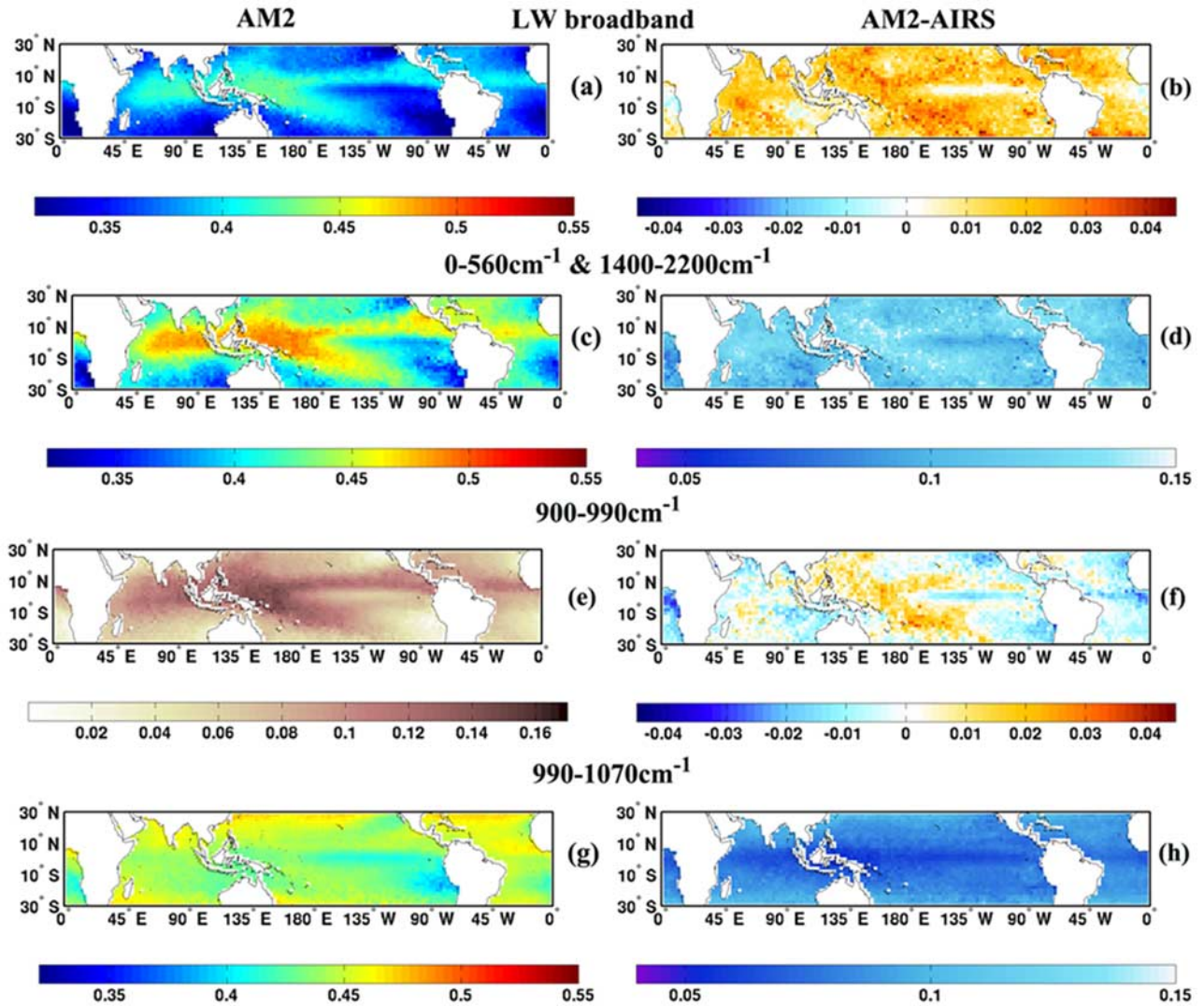[a]In practice, spectral range 1 and 8 are treated together as one combined band.

Figure 9. (a) The 2004 annual-mean broadband greenhouse parameters (g_{LW}) over the tropical oceans simulated by the AM2. (b) The difference between AM2-simulated and AIRS-inferred g_{LW}. (c)–(d) Same as Figures 9a–9b except for the spectral greenhouse parameters over the combined band of $0–560$ cm^{-1} and $1400–2200$ cm^{-1}. (e)–(f) and (g)–(h) Same as Figures 9c–9d except for spectral ranges of $560–800$ cm^{-1} and $990–1070$ cm^{-1}, respectively. Please note four different color bars, corresponding to four different sets of value range, are used here.

major continents and the central and eastern Pacific (90–180°W) in the deep tropics, regions featured with large-scale subsidence. As we shall see later, such overestimations and underestimations in the broadband g_{LW} have in fact originated from different spectral ranges.

[39] Figure 9c shows the simulated annual-mean clear-sky spectral greenhouse parameters (hereafter, $g_{\Delta\nu}$) over the combined band of $0–560$ cm^{-1} and $1400–2200$ cm^{-1} (hereafter, the combined water vapor band). Both $0–560$ cm^{-1} and $1400–2200$ cm^{-1} bands are sensitive to relative humidity over a broad vertical layer approximately from 600 hPa to 200 hPa. As a result, the $g_{\Delta\nu}$ is highly correlated with the water vapor amount in the middle and upper troposphere, with maxima over the ITCZ and SPCZ and minima over the large-scale subsidence regions. The corresponding AM2-AIRS difference shown in Figure 9d is positive over all of the tropical oceans. This suggests that

the AM2 overestimates the relative humidity in the middle and upper troposphere for the entire tropical oceans. We note here that satellite only samples the clear-sky footprints while the model output, even subsampled according to the satellite tracks, could be cloudy profiles. Therefore, such sampling difference might partly explain the differences seen in Figure 9d, especially over the convective regions. *Huang et al.* [2006] examined the same model and showed that the majority of model bias cannot be explained by such sampling difference alone. The $g_{\Delta\nu}$ in the window region (Figure 9e) is much smaller than both the g_{LW} and the $g_{\Delta\nu}$ of the combined water vapor band: the AM2-simulated $g_{\Delta\nu}$ is only $\sim0.12–0.15$ in the ITCZ and SPCZ and ~0.04 in the other tropical oceans. This is because, besides the water vapor continuum absorption, the atmosphere is almost transparent in the window region. The water vapor continuum absorption in this spectral region is proportional to the
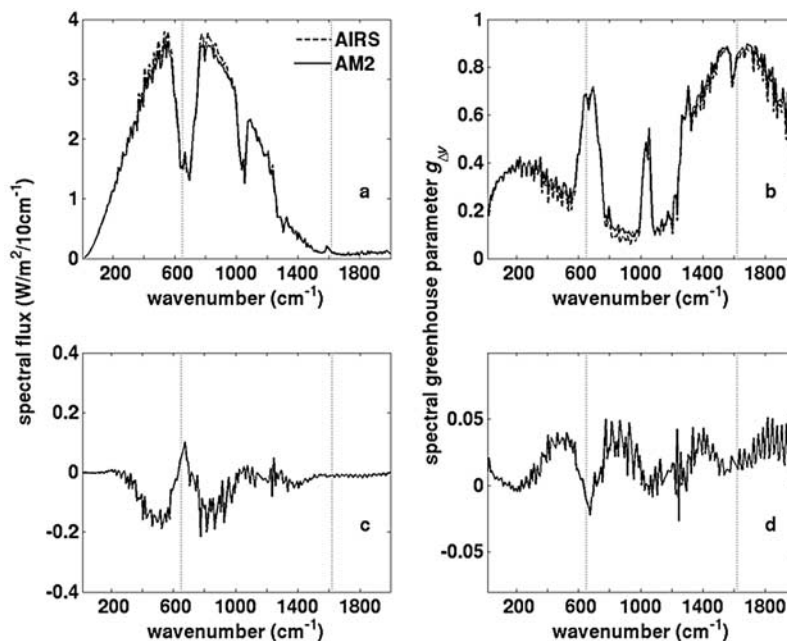
Figure 10. (a) The annual-mean clear-sky spectral flux (per 10 cm^{-1} intervals) over the tropical oceans as inferred from the AIRS and CERES collocated observations (dashed line) and simulated from MODTRAN5 based on the AM2 6-hourly output (solid line). (b) Same as Figure 10a except for annual-mean clear-sky spectral greenhouse parameters ($g_{\Delta v}$) at 10 cm^{-1} intervals. The annual-mean $g_{\Delta v}$ is derived from 12 monthly means of $g_{\Delta v}$. (c) The differences between the AM2-simulated and the AIRS-inferred spectra fluxes shown in Figure 10a. (d) The differences between the AM2 and AIRS $g_{\Delta v}$ shown in Figure 10b. The dotted gray lines indicate the start and ending frequencies of the portion of AIRS spectrum used in this study.

square of water vapor concentration, which makes it most sensitive to the water vapor concentration from the surface to ~3 km. The AM2-AIRS difference over this spectral range (Figure 9f) indicates an overestimation of ~0.02–0.04 in the large-scale convergence zones. In the large-scale subsidence regions, especially the oceans west of major continents, $g_{\Delta v}$ is underestimated by ~0.01–0.02. Same geographical patterns of the AM2-AIRS differences can be seen in other window regions as well (800–900 cm^{-1}, 1070–1200 cm^{-1}, not shown here). Such differences suggest an overestimation of the lower tropospheric (0–3 km) humidity in the large-scale convergence zones and an underestimation of it in the large-scale subsidence regions by the AM2. In the large-scale subsidence regions, the underestimation over the window regions (e.g., Figure 9f) slightly outplays the overestimation over the combined water vapor bands (Figure 9d) and other spectral ranges. As a result, the AM2 broadband g_{LW} at these regions are slightly underestimated (Figure 9b). For the large-scale convergence zones, overestimations exist in both the water vapor bands and the window regions, which leads to a ~10% overestimation in the AM2 broadband g_{LW}.

[40] Figure 9g shows the simulated $g_{\Delta v}$ for the spectral range of 990–1070 cm^{-1} (the ozone band). Unlike other spectral ranges discussed above, the simulated $g_{\Delta v}$ of this spectral range has maxima in the subtropics rather than in the deep tropics because of the higher lower stratospheric ozone concentrations in the subtropics in comparison to the deep tropics. The AM2-AIRS differences (Figure 9h) show a zonally uniform pattern with minima in the deep tropics.

Given the AM2 simulation is done with the 1990s ozone climatology, the AM2-AIRS differences here reflect (1) the difference of ozone distribution between the 1990s climatology used in the simulation and the actual ozone distribution in 2004 and (2) the lower stratospheric temperature difference between the AM2 simulation and the reality.

5.2. Comparisons of 10 cm^{-1} Spectral Fluxes

[41] When comparisons are conducted in a finer spectral resolution, 10 cm^{-1} spectral interval, further compensating differences within a given band can be revealed. Figure 10a shows the annual-mean clear-sky spectral fluxes averaged over tropical oceans for every 10 cm^{-1} interval from 10 cm^{-1} to 2000 cm^{-1} as computed from the MODTRAN5 based on the AM2 output (the solid line) and as derived from collocated AIRS and CERES observations (the dashed line). The corresponding AM2-AIRS difference is shown in Figure 10c. The corresponding annual-mean spectral greenhouse parameters are shown in Figure 10b and their differences in Figure 10d. The spectral flux difference from 10 to 300 cm^{-1} is close to zero, followed by systematic negative difference in the rest of water vapor rotational band (300–560 cm^{-1}). Correspondingly, the AM2-AIRS difference in $g_{\Delta v}$ is positive from 300 to 560 cm^{-1}. The water vapor $v2$ band (~1200–2000 cm^{-1}) has the highest $g_{\Delta v}$ (~0.6–0.85) among all spectral ranges and the difference in $g_{\Delta v}$ is also systematically positive. CO$_2$ 667 cm^{-1} band shows compensating errors from the different parts of the band: the flux ($g_{\Delta v}$) differences in the band center are positive (negative) while those in the band wings are negative
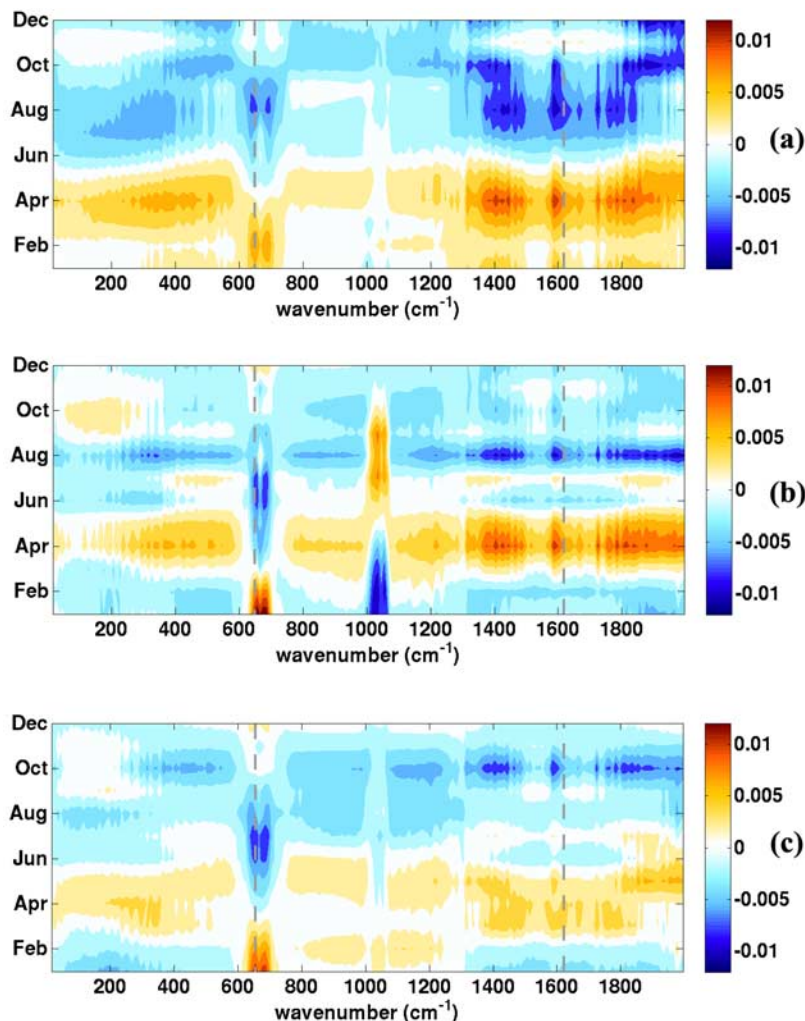
Figure 11. (a) The AM2 monthly variations of the clear-sky spectral greenhouse parameters $g_{\Delta\nu}$ (per 10 cm^{-1} interval) from the annual mean $g_{\Delta\nu}$ (the solid line in Figure 9b) as computed from MODTRAN™-5. (b) Same as Figure 11a except for the $g_{\Delta\nu}$ derived from collocated AIRS and CERES observations. (c) Same as Figure 11a except for the 2004 NCEP-DOE reanalysis 6-hourly output. The 6-hourly NCEP-DOE reanalysis is processed in a way similar to the AM2 output. The dash gray lines indicate the start and ending frequencies of the portion of AIRS spectrum used in this study.

(positive), indicating that the biases of the AM2-simulated tropospheric and stratospheric temperatures have opposite signs.

[42] Besides the annual mean $g_{\Delta\nu}$, monthly variations from the annual mean can be examined to reveal the seasonal cycle of $g_{\Delta\nu}$. Such monthly anomalies are shown in Figure 11a and 11b for the AM2 and observations, respectively. For the window regions, both the AM2 and observations show positive variations (compared to the annual mean) from January to June with maxima in April and negative anomalies in the other months with minima in August. For part of the water vapor rotational bands (300–560 cm^{-1}) and the whole water vapor v2 band, both the AM2 and observations have maximum positive variations in April. However, the observed negative anomalies over the same spectral regions peak in August while the simulated ones tend to have broad negative minima extended from August to October and even to December. For comparison, 6-hourly NCEP-DOE reanalysis (NCEP-II) data over the

same period is processed in the same way as the AM2 model output and the corresponding monthly variations of $g_{\Delta\nu}$ are shown in Figure 11c. For NCEP-II reanalysis, the negative minima in the water vapor bands are concentrated in October, different from both the AM2 simulation and the AIRS-inferred observations. This reflects differences in simulated, assimilated, and observed seasonality of tropical middle and upper troposphere relative humidity, especially in the second half year. The AM2, AIRS, and NCEP-II all reveal prominent seasonal variations of $g_{\Delta\nu}$ around the CO_2 band center (640–690 cm^{-1}) but the peaks in the AM2 lag those in the observations by 1–2 months, suggesting the discrepancies in simulating the phase of seasonal variations in the middle and lower stratospheric temperature. The NCEP-II, on the other hand, agrees with the AIRS to a large extent for both the phase and amplitude of the seasonal variations in the CO_2 band center. The AIRS exhibit a strong seasonal variation in the O_3 band center (1010–1065 cm^{-1}) with maximum in July–September and mini-

mum in January–March. This seasonal variation is primarily due to seasonal changes of ozone concentration because when a constant tropical-mean ozone profile is used in the MODTRAN5 for generating all synthetic spectral fluxes for both the AM2 and NCEP-II, such seasonal variations in the ozone band are hardly seen (Figure 11a and 11c).

[43] Sections 5.1 and 5.2 demonstrate that the spectral fluxes derived from the collocated AIRS and CERES data can be used to evaluate climate models in various ways. The band-by-band fluxes calculated in the GCM can be directly compared with the derived spectral fluxes. Compensating errors among different bands can be disclosed in this way. Also, using a narrow-band radiative transfer model like the MODTRAN5, comparison could be done at even finer spectral resolution and compensating errors within an individual band can be further revealed.

6. Conclusions and Discussions

[44] Collocated AIRS and CERES observations are used in this study to derive clear-sky outgoing spectral fluxes at 10 cm^{-1} interval from 10 to 2000 cm^{-1}. The spectral ADMs are developed based on the CERES scene types. Such ADMs are then used to convert the AIRS radiances to spectral fluxes. Fluxes over the spectral ranges not covered by the AIRS instrument are derived using a multivariate regression scheme. The algorithm is validated against synthetic spectral fluxes as well as the collocated CERES broadband OLR.

[45] Using the GFDL AM2 model as a case study, applications of the derived clear-sky spectral fluxes in GCM evaluations are also discussed. Such spectral fluxes can reveal the compensating errors that cannot be detected in the traditional comparison of the broadband OLR. Compensating errors from different broad spectral ranges as well as within a given spectral range can be quantitatively revealed. The comparisons with the AM2 simulation show how the spatial distribution and temporal evolution of water vapor at different parts of the troposphere contribute to the spectral flux differences. As shown in Figure 9, the AM2 tends to be more humid than the observations in the middle and upper troposphere for all tropical oceans. In the lower troposphere, it tends to be more humid in the large-scale convergence zones but dryer in the large-scale subsidence zones. This suggests dynamical causes of simulated water vapor biases. As for the seasonal variations of the spectral fluxes in the water vapor rotational band and $v2$ band, the AM2 model agrees with the AIRS observation and NCEP-II reanalysis for the first half year but not for the second half year: the AM2 model has broad negative variations spanning from August to October and even to December while the AIRS shows negative minima concentrated in August and the NCPE-II data has negative minima in October. Such discrepancies among model, observation, and reanalysis in the spectral domain confirm the value of infrared spectral fluxes in model evaluation.

[46] This study serves as the first step toward deriving the TOA spectral cloud radiative forcing. While temperature and humidity profiles retrieved from AIRS spectra can be used to compute the TOA clear-sky spectral fluxes, to compute TOA cloudy spectral fluxes from retrieval products is subject to more uncertainties because of the difficulty of reliably retrieving cloud properties from IR sounders. With an ultimate goal of deriving TOA spectral cloud radiative forcing, we choose to work directly with radiance measurements so the CERES-like methodology can be applied to both clear-sky and cloudy measurements consistently. Besides, AIRS retrieved temperature and humidity profiles are the averaged quantities over 3×3 AIRS footprints, which might bring additional difficulty when the OLR computed from such retrievals is to be compared with collocated CERES OLR at the single FOV level.

[47] Meanwhile, we acknowledge that in principle AIRS level-2 retrieval products alone can be used to compute spectral fluxes [*Mehta and Susskind*, 1999] independently and it has its own uniqueness [*Susskind et al.*, 2003; *Molnar and Susskind*, 2006]. The concept of effective zenith angle introduced by *Mehta and Susskind* [1999] makes it possible to compute spectral fluxes from retrieval products in an economical way. AIRS retrieval adopts a cloud-clearing approach [*Susskind et al.*, 2003]. As a result, the clear-sky flux computed from such retrieval products represents the flux that would have gone to space if the scene were otherwise identical but cloud free, which is consistent with the definition of clear-sky flux computed from the climate models. To fully investigate the application of AIRS level-2 retrieval products in deriving band-by-band flux and spectral cloud radiative forcing is beyond the scope of this study since the focus here is a radiance-to-flux approach and collocation with CERES is desired for ensuring the validity of this approach.

[48] The confidence in the spectral fluxes derived from the collocated AIRS and CERES observations depends on the accuracy of the algorithm described in section 3. Uncertainties in the derived spectral fluxes could originate from various sources. The mean spectral fluxes and the corresponding principal components used in the multivariate regression schemes have their limitations since they are derived from a set of finite samples. Another source of error exists in the forward radiative transfer modeling, MODTRAN5, especially in the far IR, a spectral range not covered by the AIRS instrument and therefore purely relying on the MODTRAN5 and the regression scheme. The importance of far-IR water vapor absorption to the clear-sky radiative budget has been long recognized [*Clough et al.*, 1992; *Sinha and Harries*, 1995, 1997]. This study has to infer the far-IR spectral fluxes since AIRS has no coverage in the far IR. Such inferences are feasible because of the redundant information content between the water vapor rotation band and the water vapor $v2$ band, the latter being largely covered by the AIRS instrument. To a large extent, the regression scheme infers the far-IR spectra fluxes through the close correlations between the two water vapor bands. With more investigative efforts on directly observing spectrally resolved radiance in the far IR from space [*Mlynczak et al.*, 2006; *Palchetti et al.*, 2006], this situation could be improved in the future by merging observations from multiple spectrometer instruments to create a merged data set of spectral fluxes over the entire thermal-IR spectral range.

References

Ackerman, S. A., et al. (1992), Radiation budget studies using collocated observations from Advanced Very High-Resolution Radiometer, High-Resolution Infrared Sounder/2, and Earth Radiation Budget Experiment instruments, *J. Geophys. Res.*, 97, 11,513–11,525.

Allan, R. P., et al. (2004), Simulation of the Earth's radiation budget by the European centre for Medium-Range Weather Forecasts 40-year reanalysis (ERA40), *J. Geophys. Res.*, 109, D18107, doi:10.1029/2004JD004816.

Anderson, G., et al. (2006), Atmospheric sensitivity to spectral top-of-atmosphere solar irradiance perturbations, using MODTRAN-5 radiative transfer algorithm, *Eos Trans. AGU*, 87(52), Fall Meet. Suppl., Abstract A11C-05.

Aumann, H. H., et al. (2003), AIRS/AMSU/HSB on the aqua mission: Design, science objectives, data products, and processing systems, *IEEE Trans. Geosci. Remote Sens.*, 41, 253–264, doi:10.1109/TGRS.2002. 808356.

Barkstrom, B. R. (1984), The Earth Radiation Budget Experiment (ERBE), *Bull. Am. Meteorol. Soc.*, 65, 1170–1185, doi:10.1175/1520-0477 (1984)065<1170:TERBE>.

Berk, A., et al. (1998), MODTRAN cloud and multiple scattering upgrades with application to AVIRIS, *Remote Sens. Environ.*, 65, 367–375, doi:10.1016/S0034-4257(98)00045-5.

Berk, A., et al. (2005), MODTRAN5: A reformulated atmospheric band model with auxiliary species and practical multiple scattering options, *Proc. SPIE Int. Soc. Opt. Eng.*, 5655, 88.

Bernstein, L. S., et al. (1996), Very narrow band model calculations of atmospheric fluxes and cooling rates, *J. Atmos. Sci.*, 53, 2887–2904, doi:10.1175/1520-0469(1996)053<2887:VNBMCO>.

Chahine, M. T., et al. (2006), AIRS: Improving weather forecasting and providing new data on greenhouse gases, *Bull. Am. Meteorol. Soc.*, 87, 911–926, doi:10.1175/BAMS-87-7-911.

Clough, S. A., and M. J. Iacono (1995), Line-by-line calculation of atmospheric fluxes and cooling rates: 2. Application to carbon dioxide, ozone, methane, nitrous oxide and the halocarbons, *J. Geophys. Res.*, 100, 16,519–16,535, doi:10.1029/95JD01386.

Clough, S. A., et al. (1992), Line-by-line calculations of atmospheric fluxes and cooling rates: Application to water vapor, *J. Geophys. Res.*, 97, 15,761–15,785.

Clough, S. A., et al. (2005), Atmospheric radiative transfer modeling: A summary of the AER codes, *J. Quant. Spectrosc. Radiat. Transf.*, 91, 233–244, doi:10.1016/j.jqsrt.2004.05.058.

DAO (1996), *Algorithm Theoretical Basis Document for Goddard Earth Observing System Data Assimilation System (GOES DAS) With a Focus Version 2*, 310 pp., Data Assimilation Off., NASA Goddard Space Flight Cent., Greenbelt, Md.

Feldman, D. R., et al. (2006), Direct retrieval of stratospheric CO2 infrared cooling rate profiles from AIRS data, *Geophys. Res. Lett.*, 33, L11803, doi:10.1029/2005GL024680.

Freidenreich, S. M., and V. Ramaswamy (1999), A new multiple-band solar radiative parameterization for general circulation models, *J. Geophys. Res.*, 104, 31,389–31,409, doi:10.1029/1999JD900456.

Frey, R. A., et al. (1996), Climate parameters from satellite spectral measurements. 1. Collocated AVHRR and HIRS/2 observations of spectral greenhouse parameter, *J. Clim.*, 9, 327–344, doi:10.1175/1520-0442 (1996)009<0327:CPFSSM>2.0.CO;2.

Gaiser, S. L., et al. (2003), In-flight spectral calibration of the atmospheric infrared sounder, *IEEE Trans. Geosci. Rem. Sens.*, 41, 287–297, doi:10.1109/TGRS.2003.809708.

Geier, E. B., et al. (2001), *Single Satellite Footprint TOA/Surface Fluxes and Clouds (SSF) Collection Documents*, 243 pp., Clim. Sci. Branch, NASA Langley Res. Cent., Hampton, Va. (Available at http://asd-www.larc.nasa.gov/ceres/collect_guide/SSF-CG.pdf)

GFDL Global Atmosphere Model Development Team (2004), The new GFDL global atmosphere and land model AM2–LM2: Evaluation with prescribed SST simulations, *J. Clim.*, 17, 4641–4673, doi:10.1175/JCLI-3223.1.

Goodberlet, M. A., et al. (1990), Ocean surface wind-speed measurements of the Special Sensor Microwave Imager (SSM/I), *IEEE Trans. Geosci. Remote Sens.*, 28, 823–828, doi:10.1109/36.58969.

Goody, R., et al. (1998), Testing climate models: An approach, *Bull. Am. Meteorol. Soc.*, 79, 2541–2549, doi:10.1175/1520-0477(1998)079<2541:TCMAA>2.0.CO;2.

Harries, J. E., et al. (2005), The Geostationary Earth Radiation Budget (GERB) project, *Bull. Am. Meteorol. Soc.*, 86, 945–960, doi:10.1175/BAMS-86-7-945.

Haskins, R., et al. (1999), Radiance covariance and climate models, *J. Clim.*, 12, 1409–1422, doi:10.1175/1520-0442(1999)012<1409:RCACM>2.0.CO;2.

Horowitz, L. W. (2006), Past, present, and future concentrations of tropospheric ozone and aerosols: Methodology, ozone evaluation, and sensitivity to aerosol wet removal, *J. Geophys. Res.*, 111, D22211, doi:10.1029/2005JD006937.

Houze, R. A. (1993), *Cloud Dynamics*, 573 pp., Elsevier, New York.

Huang, X. L., and Y. L. Yung (2005), Spatial and spectral variability of the outgoing thermal IR spectra from AIRS: A case study of July 2003, *J. Geophys. Res.*, 110, D12102, doi:10.1029/2004JD005530.

Huang, X. L., J. J. Liu, and Y. L. Yung (2003), Analysis of thermal emission spectrometer data using spectral EOF and tri-spectral methods, *Icarus*, 165, 301–314, doi:10.1016/S0019-1035(03)00206-9.

Huang, X. L., V. Ramaswamy, and M. D. Schwarzkopf (2006), Quantification of the source of errors in AM2 simulated tropical clear-sky outgoing longwave radiation, *J. Geophys. Res.*, 111, D14107, doi:10.1029/2005JD006576.

Huang, Y., V. Ramaswamy, X. L. Huang, Q. Fu, and C. Bardeen (2007), A strict test in climate modeling with spectrally resolved radiances: GCM simulation versus AIRS observations, *Geophys. Res. Lett.*, 34, L24707, doi:10.1029/2007GL031409.

Kanamitsu, M., et al. (2002), NCEP-DOE AMIP-II reanalysis (R-2), *Bull. Am. Meteorol. Soc.*, 83, 1631–1643, doi:10.1175/BAMS-83-11-1631(2002)083<1631:NAR>2.3.CO;2.

Loeb, N. G., et al. (2001), Determination of unfiltered radiances from the clouds and the Earth's Radiant Energy System instrument, *J. Appl. Meteorol.*, 40, 822–835, doi:10.1175/1520-0450(2001)040<0822:DOURFT>2.0.CO;2.

Loeb, N. G., et al. (2003), Angular distribution models for top-of-atmosphere radiative flux estimation from the clouds and the Earth's Radiant Energy System instrument on the Tropical Rainfall Measuring Mission satellite. part I: Methodology, *J. Appl. Meteorol.*, 42, 240–265, doi:10.1175/1520-0450(2003)042<0240:ADMFTO>2.0.CO;2.

Loeb, N. G., et al. (2005), Angular distribution models for top-of-atmosphere radiative flux estimation from the Clouds and the Earth's Radiant Energy System instrument on the Terra satellite. Part I: Methodology, *J. Atmos. Ocean. Technol.*, 22, 338–351, doi:10.1175/JTECH1712.1.

Loeb, N. G., et al. (2007), Angular distribution models for top-of-atmosphere radiative flux estimation from the Clouds and the Earth's Radiant Energy System instrument on the Terra satellite. Part II: Validation, *J. Atmos. Ocean. Technol.*, 24, 564–584, doi:10.1175/JTECH1983.1.

Mann, M. E., R. S. Bradley, and M. K. Hughes (1998), Global-scale temperature patterns and climate forcing over the past six centuries, *Nature*, 392, 779–787, doi:10.1038/33859.

Mehta, A., and J. Susskind (1999), Outgoing longwave radiation from the TOVS Pathfinder Path A data set, *J. Geophys. Res.*, 104(D10), 12,193–12,212, doi:10.1029/1999JD900059.

Mlynczak, M. G., et al. (2006), First light from the Far-Infrared Spectroscopy of the Troposphere (FIRST) instrument, *Geophys. Res. Lett.*, 33, L07704, doi:10.1029/2005GL025114.

Molnar, G. I., and J. Susskind (2006), Satellite sounder-based OLR-, cloud- and atmospheric temperature climatologies for climate analyses, in *Algorithms and Technologies for Multispectral, Hyperspectral, and Ultraspectral Imagery XII*, edited by S. S. Shen and P. E. Lewis, *Proc. SPIE Int. Soc. Opt. Eng.*, 6233, 62331D.

Pagano, T. S., et al. (2003), Prelaunch and in-flight radiometric calibration of the Atmospheric Infrared Sounder (AIRS), *IEEE Trans. Geosci. Remote Sens.*, 41, 265–273, doi:10.1109/TGRS.2002.808324.

Palchetti, L., et al. (2006), Technical note: First spectral measurement of the Earth's upwelling emission using an uncooled wideband Fourier transform spectrometer, *Atmos. Chem. Phys.*, 6, 5025–5030.

Parkinson, C. L. (2003), Aqua: An earth-observing satellite mission to examine water and other climate variables, *IEEE Trans. Geosci. Remote Sens.*, 41, 173–183, doi:10.1109/TGRS.2002.808319.

Ramanathan, V., et al. (1989), Cloud-radiative forcing and climate: Results from the Earth Radiation Budget Experiment, *Science*, 243, 57–63, doi:10.1126/science.243.4887.57.

Randel, W. J., and F. Wu (2007), A stratospheric ozone profile data set for 1979–2005: Variability, trends, and comparisons with column ozone data, *J. Geophys. Res.*, 112, D06313, doi:10.1029/2006JD007339.

Raval, A., and V. Ramanathan (1989), Observational determination of the greenhouse effect, *Nature*, 342, 758–761, doi:10.1038/342758a0.

Raval, A., et al. (1994), Observed dependence of outgoing longwave radiation on sea-surface temperature and moisture, *J. Clim.*, 7, 807–821, doi:10.1175/1520-0442(1994)007<0807:ODOOLR>2.0.CO;2.

Rothman, L. S., et al. (1998), The HITRAN molecular spectroscopic database and HAWKS (HITRAN Atmospheric Workstation): 1996 edition, *J. Quant. Spectrosc. Radiat. Transfer*, 60, 665–710, doi:10.1016/S0022-4073(98)00078-8.

Rothman, L. S., et al. (2005), The HITRAN 2004 molecular spectroscopic database, *J. Quant. Spectrosc. Radiat. Transfer*, 96, 139–204, doi:10.1016/j.jqsrt.2004.10.008.

Schwarzkopf, M. D., and V. Ramaswamy (1999), Radiative effects of CH4, N2O, halocarbons and the foreign-broadened H2O continuum: A GCM experiment, *J. Geophys. Res.*, 104, 9467–9488, doi:10.1029/1999JD900003.

Sinha, A., and J. E. Harries (1995), Water vapor and greenhouse trapping: The role of far-infrared absorption, *Geophys. Res. Lett.*, 22, 2147–2150, doi:10.1029/95GL01891.

Sinha, A., and J. E. Harries (1997), The Earth's clear-sky radiation budget and water vapor absorption in the far infrared, *J. Clim.*, 10, 1601–1614, doi:10.1175/1520-0442(1997)010<1601:TESCSR>2.0.CO;2.

Slingo, A., and M. J. Webb (1992), Simulation of clear-sky outgoing longwave radiation over the oceans using operational analyses, *Q. J. R. Meteorol. Soc.*, 118, 1117–1144, doi:10.1002/qj.49711850806.

Slingo, A., et al. (1998), A 15-year simulation of the clear-sky greenhouse effect using the ECMWF reanalyses: Fluxes and comparisons with ERBE, *J. Clim.*, 11, 690–708, doi:10.1175/1520-0442(1998)011<0690:AYSOTC>2.0.CO;2.

Strow, L. L., et al. (2003), Prelaunch spectral calibration of the Atmospheric Infrared Sounder (AIRS), *IEEE Trans. Geosci. Remote Sens.*, 41, 274–286, doi:10.1109/TGRS.2002.808245.

Strow, L. L., et al. (2006), Validation of the Atmospheric Infrared Sounder radiative transfer algorithm, *J. Geophys. Res.*, 111, D09S06, doi:10.1029/2005JD006146.

Susskind, J., C. D. Barnet, and J. M. Blaisdell (2003), Retrieval of atmospheric and surface parameters from AIRS/AMSU/HSB data in the presence of clouds, *IEEE Trans. Geosci. Remote Sens.*, 41, 390–409, doi:10.1109/TGRS.2002.808236.

Uppala, S. M., et al. (2005), The ERA-40 re-analysis, *Q. J. R. Meteorol. Soc.*, 131, 2961–3012, doi:10.1256/qj.04.176.

Wielicki, B. A., et al. (1996), Clouds and the Earth's radiant energy system (CERES): An Earth observing system experiment, *Bull. Am. Meteorol. Soc.*, 77, 853–868, doi:10.1175/1520-0477(1996)077<0853:CATERE>2.0.CO;2.

Wielicki, B. A., et al. (2002), Evidence for large decadal variability in the tropical mean radiative energy budget, *Science*, 295, 841–844, doi:10.1126/science.1065837.

Yang, S. K., et al. (1999), Evaluation of the earth radiation budget in NCEP-NCAR reanalysis with ERBE, *J. Clim.*, 12, 477–493, doi:10.1175/1520-0442(1999)012<0477:EOTERB>2.0.CO;2.

―――――――――――――

X. Huang, Department of Atmospheric, Oceanic, and Space Sciences, University of Michigan, 2455 Hayward Street, Ann Arbor, MI 48109-2143, USA.

N. G. Loeb, Radiation and Climate Branch, NASA Langley Research Center, Hampton, VA 23681-2199, USA.

V. Ramaswamy, Geophysical Fluid Dynamics Laboratory, NOAA, Princeton University Forrestal Campus, Princeton, NJ 08542, USA.

W. Yang, Now at Hunter College, City University of New York, 695 Park Avenue, New York, NY 10065, USA.